remote sensing

MDPI

Article

Quantifying Changes in Groundwater Storage and Response to Hydroclimatic Extremes in a Coastal Aquifer Using Remote Sensing and Ground-Based Measurements: The Texas Gulf Coast Aquifer

Bimal Gyawali *, Dorina Murgulet and Mohamed Ahmed

Center for Water Supplies Studies, Department of Physical and Environmental Sciences, Texas A & M University-Corpus Christi, 6300 Ocean Drive, Corpus Christi, TX 78412, USA; dorina.murgulet@tamucc.edu (D.M.); mohamed.ahmed@tamucc.edu (M.A.)
* Correspondence: bgyawali@islander.tamucc.edu; Tel.: +1-361-825-2309

Abstract: With the increasing vulnerability of groundwater resources, especially in coastal regions, there is a growing need to monitor changes in groundwater storage (GWS). Estimations of GWS have been conducted extensively at regional to global scales using GRACE and GRACE-FO observations. The major goal of this study was to evaluate the applicability of uninterrupted monthly GRACE-derived terrestrial water storage (TWS_{GRACE}) records in facilitating detection of long- and short-term hydroclimatic events affecting the GWS in a coastal area. The TWS_{GRACE} data gap was filled with reconstructed values from multi-linear regression (MLR) and artificial neural network (ANN) models and used to estimate changes in GWS in the Texas coastal region (Gulf Coast and Carrizo–Wilcox Aquifers) between 2002 and 2019. The reconstructed TWS_{GRACE}, along with soil moisture storage (SMS) from land surface models (LSMs), and surface water storage (SWS) were used to estimate the GRACE-derived GWS (GWS_{GRACE}), validated against the GWS estimated from groundwater level observations (GWS_{well}) and extreme hydroclimatic event records. The results of this study show: (1) Good agreement between the predicted TWS_{GRACE} data gaps from the MLR and ANN models with high accuracy of predictions; (2) good agreement between the GWS_{GRACE} and GWS_{well} records (CC = 0.56, p-value < 0.01) for the 2011–2019 period for which continuous GWL_{well} data exists, thus validating the approach and increasing confidence in using the reconstructed TWS_{GRACE} data to monitor coastal GWS; (3) a significant decline in the coastal GWS_{GRACE}, at a rate of 0.35 ± 0.078 km^3·yr^{-1} (p-value < 0.01), for the 2002–2019 period; and (4) the reliable applicability of GWS_{GRACE} records in detecting multi-year drought and wet periods with good accuracy: Two drought periods were identified between 2005–2006 and 2010–2015, with significant respective depletion rates of -8.9 ± 0.95 km^3·yr^{-1} and -2.67 ± 0.44 km^3·yr^{-1} and one wet period between 2007 and 2010 with a significant increasing rate of 2.6 ± 0.63 km^3·yr^{-1}. Thus, this study provides a reliable approach to examine the long- and short-term trends in GWS in response to changing climate conditions with significant implications for water management practices and improved decision-making capabilities.

Keywords: groundwater storage; GRACE; Texas; coastal terrestrial water storage; hydroclimatic extreme events

Citation: Gyawali, B.; Murgulet, D.; Ahmed, M. Quantifying Changes in Groundwater Storage and Response to Hydroclimatic Extremes in a Coastal Aquifer Using Remote Sensing and Ground-Based Measurements: The Texas Gulf Coast Aquifer. *Remote Sens.* **2022**, *14*, 612. https://doi.org/10.3390/rs14030612

Academic Editors: Jolanta Nastula and Monika Birylo

Received: 17 December 2021
Accepted: 25 January 2022
Published: 27 January 2022

1. Introduction

Groundwater is the main source of freshwater for almost half of the world's population; it provides a major resource for irrigation and plays a key role in ecosystem health [1,2]. Yet, groundwater resources are under extreme threat due to rapid depletion [3–6], a serious global issue affecting groundwater resource sustainability and ecosystem health. Global groundwater storage (GWS) decreased by 4500 km^3 (~42 km^3·yr^{-1}) between 1900 and 2008,

with a significant acceleration in the depletion rate since 1950. The depletion rate more than tripled (~145 $km^3 \cdot yr^{-1}$) between 2000 and 2008 [7]. During the same period, in the United States (U.S.) GWS decreased by 1000 km^3 (~9.3 $km^3 \cdot yr^{-1}$) and the rate doubled after 2000 (~24 $km^3 \cdot yr^{-1}$) [8].

Groundwater is often the only source of freshwater in coastal areas. This source, however, is vulnerable to climate and anthropogenic variabilities. Coastal regions are among the most densely populated areas that place an increasing demand on coastal aquifers [9–11] associated with ever-growing agricultural irrigation and industrial needs. Seawater intrusion, for example, could result from excessive pumping [3,12–14], storm surge [14–16], and/or sea level rise [17,18]. Coastal aquifers are more vulnerable to depletion due to excessive groundwater extraction when compared to sea level rise [19]. Where groundwater extraction is high, coastal areas experience seawater intrusion, also exacerbated by the sea level rise, and coastal land subsidence [17,20]. Storms may lead to an increase in water table levels and flooding because of either high surge or larger volumes of precipitations [15].

Historically, groundwater monitoring relied mainly on field observations of groundwater levels (GWL) from monitoring wells. Estimations of GWS from field observations have shown significant seasonal and annual variations in areas where observations are relatively dense [21,22]. However, in many parts of the world spatial and temporal coverage of groundwater level measurements are sparse [23,24]. While the U.S. has a relatively dense well observation network, more monitoring sites are required for improved understanding of the GWS spatial and temporal patterns in relation to groundwater extraction [25]. In addition, monitoring GWS using in situ measurements is a relatively expensive and labor-intensive process [26]. When in situ measurements are not adequate for temporal and spatial coverage, satellite observations play a significant role in GWS monitoring (e.g., recharge, discharge, and storage changes) [6,27–29]. Data from the Gravity Recovery and Climate Experiment (GRACE; 2002–2017) and its successor GRACE-Follow On (GRACE-FO; 2018–present) missions [30,31] have been shown to overcome the above-mentioned limitations.

GRACE, a joint U.S.–German satellite mission, was launched, in March 2002, to monitor the spatial and temporal variations in the Earth's gravity field [30]. These variations have been converted to changes in terrestrial water storage (TWS), after removing atmospheric mass variations and ocean tides. Storage components of the TWS are soil moisture, surface water, snow/ice, and groundwater [32]. GRACE-derived TWS (TWS_{GRACE}) together with land surface models (LSM) and ground-based measurements (e.g., GWL) have been widely used to monitor GWS around the world, including the Mississippi River basin [33], the Central Valley of California [12], northwestern India [34], Africa [6,35–38], Asia [39], and northern China [40,41]. These studies also have shown a good agreement between GRACE-derived GWS (GWS_{GRACE}) and GWL-derived GWS (GWS_{well}) in different geologic and hydrogeologic settings [27,28,40,42].

After the GRACE mission ended in June 2017, the next generation of GRACE, GRACE-FO mission, launched in May 2018 [31]. As with its predecessor, the GRACE-FO observations have been successfully applied in TWS_{GRACE} estimations. However, there are temporal gaps between the GRACE and GRACE-FO missions (11 months; 7/2017 to 5/2018) as well as within TWS_{GRACE} record (22 months: 06/2002, 07/2002, 06/2003, 01/2011, 06/2011, 05/2012, 10/2012, 03/2013, 08/2013, 09/2013, 02/2014, 07/2014, 12/2014, 06/2015, 10/15, 11/2015, 04/2016, 09/2016, 10/2016, 02/2017, 08/2018, and 09/2018) due to failure in battery performance of the GRACE satellites [43].

Effective planning and management of groundwater resources is largely dependent on the analysis of TWS and GWS temporal changes. However, the precision of short- and long-term spectral and statistical analysis of these timeseries depends on their continuity [43–45]. Temporal data gaps in TWS could increase the error and uncertainty in the analysis of seasonal and annual cycles as well as the short- and long-term trends [43,46,47]. Therefore, bridging gaps in TWS_{GRACE} data helps enhance performance of TWS and GWS monitoring and the outcomes that inform and improve groundwater management practices.

Several studies have used outputs of LSMs and global hydrologic models to fill gaps in TWS_{GRACE} [48–50]. However, these models cannot fully simulate influences from anthropogenic factors that affect the TWS_{GRACE} such as deep groundwater extraction and cropland irrigation [51]. Machine learning-based models have been widely used to predict hydrological variables [51–56]. Recently, reconstruction of TWS_{GRACE} data gaps on regional to global scales has been conducted using simple regression and machine learning techniques [43,57–59]. These techniques have also been used to fill gaps in, and downscale, TWS_{GRACE} records [60–63]. However, none of the previous studies have used a gap filled TWS_{GRACE} record to examine TWS and GWS temporal variability over the Texas Gulf Coast region (Figure 1).

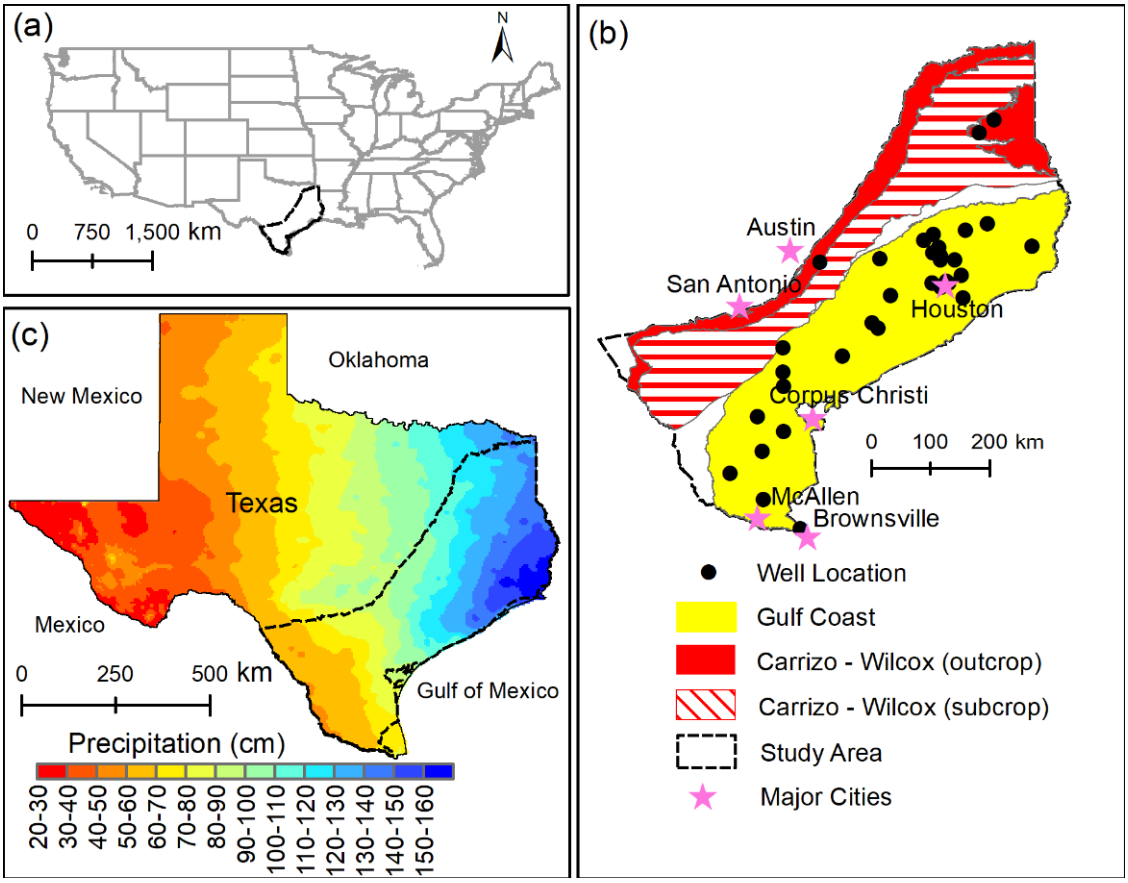

Figure 1. Study Area: (**a**) Location of the study area, (**b**) location of groundwater wells used in this study, and (**c**) precipitation climatology (1980–2010) [64].

In this study, a complete GRACE and GEACE-FO record (2002–2019) is used to characterize the temporal variability in TWS_{GRACE} and GWS_{GRACE} over the Texas Gulf Coast region (Figure 1). Specifically, the TWS_{GRACE} was first reconstructed using multi-linear regression (MLR) and artificial neural network (ANN) techniques to fill the data gaps within GRACE mission and between GRACE and GRACE-FO missions. Second, the complete TWS_{GRACE} data along with soil moisture storage (SMS) from LSMs, and surface water storage (SWS) were used to derive the GWS_{GRACE} timeseries. The GWS_{wel} was also estimated using GWLs and used to validate the GWS_{GRACE} estimates. Our short-term and long-term trend analysis of complete TWS_{GRACE} and GWS_{GRACE} datasets provided a quantitative means to identify the short and multi-year drought and wet periods with significant accuracy, thus enabling enhanced decision-making processes of a broad set of water planning groups and stakeholders.

2. Material and Methods

2.1. Study Area

Nearly 40% of Texas's population live in the Gulf Coast region [65]. The Gulf Coast Aquifer (GCA) and Carrizo–Wilcox Aquifer (CWA), extending from South Texas northeastward into East Texas (approximate four corner coordinates: (29, −100.6), (26, −97.6), (33.5, −94), and (30, −93.5)), are among the major aquifers of Texas (Figure 1). These two aquifers provide an important source of freshwater for agriculture, municipal, and domestic uses.

The GCA encompasses approximately 110,000 km^2 and is composed of multiple aquifer units comprised of a series of discontinuous sand, silt, clay, and gravel beds of Miocene to Holocene age [66,67]. Groundwater in GCA is mostly unconfined and semi-confined. Freshwater saturated thickness ranges from 213 m (to the south) to 396 m (to the north) with an average of about 305 m. The hydraulic conductivity of the aquifer is about 0.3 $m \cdot day^{-1}$ in the southern area and as much as 2.1 $m \cdot day^{-1}$ in the northeast [68]. Because of smaller saturated depth and lower hydraulic conductivity, aquifer transmissivity is lower in the south and maximum in the northeast. The specific yield ranges from 0.05 to 0.005, which is relatively low compared to the typical specific yields of sedimentary formations in unconfined aquifers [69].

The CWA, encompassing approximately 95,000 km^2, extends from the Louisiana border to Mexico to the northwest of GCA. The CWA consists of sand locally interbedded with gravel, silt, clay, and lignite with average saturated freshwater thickness of about 204 m. The aquifer is unconfined in the outcrop area and confined down deep towards the coast where it is overlaid by low-permeability layers. The transmissivity and hydraulic conductivity of the CWA are highly variable spatially, with a geometric mean of 28 $m^2 \cdot d^{-1}$ and 1.8 $m \cdot d^{-1}$, respectively [70].

The study area encompasses a significant climate gradient from east to west, with an average annual precipitation over 140 cm, in the east, to less than 76 cm, in southwest Texas. The rate of annual gross lake evaporation increases from 127 cm, in the east, to more than 165 cm, in southwest Texas [71]. The mean annual potential evapotranspiration (ET) exceeds precipitation by 2–5 times. Thornthwaite's water-balance system [72] classified the climate of this region as moist subhumid in the east and subtropical semiarid in the southwest.

2.2. Data

Multiple datasets from different sources were used to fill gaps in the TWS_{GRACE} record, extract and validate GWS_{GRACE} timeseries, and characterize temporal variabilities in TWS_{GRACE} and GWS_{GRACE} data over the study area (Figure 1). Below is a detailed description of datasets used in this study.

2.2.1. Terrestrial Water Storage

Terrestrial Water Storage from GRACE (TWS_{GRACE})

The 2002–2019 TWS_{GRACE} data used in this study were derived from the GRACE and GRACE-FO spherical harmonic (SH) and mass concentration (mascon) solutions provided by NASA's Jet Propulsion Laboratory (JPL), Center for Space Research (CSR), and GeoForschungsZentrum (GFZ). The five different solutions were used to check if the temporal variabilities in TWS and GWS and associated drought/flood signals were represented in all of them. The level-3 release 6 (RL06) SH solutions from CSR (CSR SH), JPL (JPL SH), and GFZ (GFZ SH) are provided at a spatial resolution of 1° × 1° [73]. The RL06 mascon solution is provided by CSR (CSR-M) and JPL (JPL-M) [74,75] with a spatial resolution of 0.25° × 0.25° and 0.5° × 0.5°, respectively.

The GRACE mission provides a scale factor for the SH and JPL-M solutions. This scale factor was used to rescale the individual TWS_{GRACE} data to minimize the signal attenuation during post-processing [73,76]. The gridded TWS_{GRACE} GRACE products were averaged over the study area to generate the TWS_{GRACE} timeseries. The average TWS_{GRACE} timeseries was calculated by taking an average of all five TWS_{GRACE} SH and mascon solutions. This average tends to minimize the noise in the individual TWS_{GRACE} solutions within

the available scatter of the solutions [77]. The gaps in the average TWS_{GRACE} timeseries (missing months and the gap between GRACE and GRACE-FO missions) were filled with the reconstructed TWS from the ANN and MLR models (refer to the "Methods" section).

Terrestrial Water Storage from Land Surface Model (TWS_{LSM})

The TWS data was also derived from the North American Land Data Assimilation System (NLDAS)-NOAH model (TWS_{LSM}). The TWS_{LSM} from NLDAS-NOAH and Global Land Data Assimilation System (GLDAS)-NOAH in the study region looks similar; therefore, we only used the TWS_{LSM} record derived from NLDAS-NOAH. This estimate was used as one of the MLR and ANN model's inputs. In this model, the TWS_{LSM} is represented as the sum of soil moisture storage (SMS), plant canopy water storage, and accumulated snow. The TWS_{LSM} was provided at a spatial resolution of $0.125^{\circ} \times 0.125^{\circ}$. The NLDAS model details are explained in Section 2.2.2 below.

2.2.2. Soil Moisture Storage (SMS)

The SMS data were extracted from the Global Land Data Assimilation System (GLDAS) and NLDAS. These two LSMs were developed jointly by the National Aeronautics and Space Administration [14] and the National Oceanic and Atmospheric Administration (NOAA). GLDAS and NLDAS simulate satellite and ground-based measurements to produce an optimal field of land surface statistics using advanced land surface modeling and data assimilation techniques [78,79]. Both models provide SMS data for different layer structures extending from the ground surface up to 3 m depth. The NLDAS derived SMS has a higher spatial resolution (i.e., 0.125°) than GLADS (i.e., 1°). Timeseries of SMS were extracted from the NOAH [80], Mosaic [81], and variable infiltration capacity (VIC) [82] model versions.

The gridded SMS data were averaged over the study area to generate SMS timeseries from each of the six model versions. Like TWS_{GRACE}, the SMS anomaly was calculated by removing the 2004–2009 temporal mean. The average of all six SMS products and their respective monthly standard deviations were used to estimate the monthly SMS timeseries and associated errors, respectively [33,83].

2.2.3. Surface Water Storage (SWS)

The SWS data extracted from the Texas Water Development Board (TWDB) (available at https://waterdatafortexas.org/reservoirs/statewide; accessed on 10 March 2020), implemented herein, provide daily lake and reservoir levels within Texas. To calculate SWS timeseries, first, the available lake and reservoir levels (total: 29) within the study region were compiled into individual monthly timeseries (i.e., for each lake/reservoir). Then, the 2004–2009 mean was removed from each timeseries. Finally, all storage anomalies were added and divided by the study area to derive the average SWS timeseries. The monthly uncertainty was estimated using a conservative approach, which is 10% of the monthly SWS [83,84].

2.2.4. Groundwater Level Observations (GWL_{well}) and Groundwater Extraction Rates

Groundwater level data from the U.S. Geological Survey (USGS) and the TWDB (available at https://waterdatafortexas.org/groundwater; accessed on 15 March 2020) were used in this study to derive the GWL_{well}. For this purpose, water level data from wells screened only in the unconfined or semi-confined portion of the GCA and CWA were selected as representative of the local water table [33]. Well hourly GWL_{well} data was aggregated into monthly timeseries. Since most of the GWL_{well} are available starting 2011, the temporal mean of the 2012–2016 period was removed from each timeseries. To ensure consistency for comparison purposes, the same time mean was removed from TWS_{GRACE}, SMS, and SWS data when compared with GWL_{well}.

The annual groundwater pumping data by county, available up to 2018, was extracted from the TWDB (available at http://www.twdb.texas.gov/waterplanning/waterusesurvey/historical-pumpage.asp; accessed on 20 March 2020).

2.2.5. Precipitation and Temperature

Precipitation and temperature data were used as one of the MLR and ANN model inputs. Precipitation data was derived from the Integrated Multi-satellite Retrievals for Global Precipitation Measurement Mission (IMERG) data products (available at https://disc.gsfc.nasa.gov/datasets/GPM_3IMERGM_06/; accessed on 1 April 2020). The IMERG provides globally half-hourly, daily, and monthly precipitation products, on a 0.1° × 0.1° grid scale [85] and is available beginning with 2000 until present.

The monthly 2-m air temperature data from the European Centre for Medium-Range Weather Forecasts (ECMWF) Re-Analysis (ERA5-Land) project was used in this study. The ERA5-Land data, available from 1950 to the present (at https://cds.climate.copernicus.eu/; accessed on 1 April 2020), are produced by the replay of the land component of the ECMWF ERA5 climate reanalysis, forced by meteorological fields from ERA5. The ERA5-Land global data have a temporal and spatial resolution of 1 h and 0.1° × 0.1°, respectively [86].

2.3. Methods

Three main steps were utilized in this study (Figure 2). First, we filled the TWS_{GRACE} data gap using predictions from the ANN and MLR models. Secondly, the complete TWS_{GRACE}, SWS, and SMS timeseries were used to extract GWS_{GRACE} timeseries over the study area. The third step included validation of the generated GWS_{GRACE} timeseries using GWS_{well} data. The temporal variability in TWS_{GRACE} and GWS_{GRACE} was characterized over the Texas Gulf Coast region using short- and long-term trend analyses.

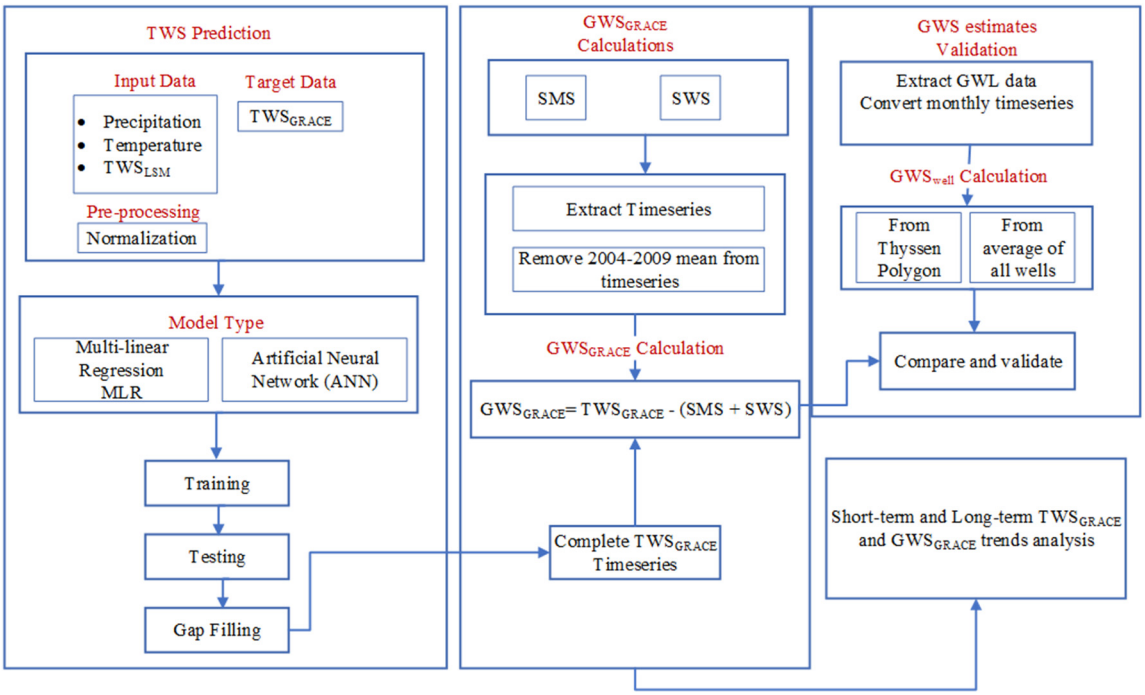

Figure 2. General flowchart showing data and methods used in this study.

2.3.1. Terrestrial Water Storage Reconstruction

The predicted values from the ANN and MLR models were used to fill in the gaps in the average TWS_{GRACE} timeseries using the following reasoning. The MLR model performs best when there is a linear relationship between target and input variables. This model has

been used widely in hydrology and meteorology [43,57,87,88] because of its simplicity. The MLR model can be explained by the following equation:

$$Y = a_0 + a_1x_1 + a_2x_2 + a_3x_3 + \ldots\ldots\ldots\ldots\ldots + a_nx_n \quad (1)$$

where Y is the target variable; x_1, x_2, x_3, and x_n are the input variables; a_0 is a constant; and a_1, a_2, a_3, and a_n are the regression coefficients.

The ANN model development is inspired by the function of biological neural networks. Such systems are trained to perform by considering examples, generally without task-specific programming [89]. The ANN model consists of input, hidden, and output layers. The number of hidden layers depends on the relationship between target and input variables. ANNs have been widely used in hydroclimatic predictions because they can handle large, non-linear, and complex datasets [43]. In this study, the number of hidden layers in the ANN model was selected by a trial-and-error method. The model was run for hidden layers from 1 to 8. The number of layers at which the model performed best (i.e., 5) was selected.

Both MLR and ANN models require target and input variables. The average TW_{GRACE} from five different solutions was used as a target variable while the precipitation, temperature, and TWS_{LSM} were selected as input variables. The input variables were normalized to ensure that all variables receive equal consideration using Equation (2):

$$\hat{x}_i = \frac{x_i - x_{min}}{x_{max} - x_{min}} \quad (2)$$

where $\hat{x}_i$ is normalized value for x_i and x_{min} and x_{max} are minimum and maximum value for the timeseries, respectively.

The ANN and MLR models were trained, tested, and validated using randomly selected data sets. The data were randomly divided into training (70%), testing (15%), and validation (~15%), with the missing months in the GRACE data and the gap between the two used for prediction purposes. To ensure the model stability, identify the associated uncertainty, and enhance model generalization, 100 simulations were run for the ANN model. The median and the standard deviation of these simulations were used as the ANN model output and as a measure of model uncertainty, respectively.

The performance of both ANN and MLR models was tested using a number of statistical criteria such as: The root mean square error (RMSE), the normalized RMSE (NRMSE), the correlation coefficient (CC), and the Nash–Sutcliffe efficiency coefficient (Equations (3)–(6)). RMSE was used to measure the global fitness of a predictive model and the optimal value is 0. The NRMSE was calculated as the normalized RMSE by the standard deviation of actual values. The cross-correlation between actual and predicted values was measured by the CC. The NSE is a normalized statistical coefficient that measures the relative magnitude of residual variance to the variance of actual/measured data [90]. The NSE value ranged from $-\infty$ to 1 with an optimal value of 1. These statistical measures were calculated as follows:

$$RMSE = \sqrt{\frac{\sum_{i=1}^{n}(y_i - x_i)}{n}} \quad (3)$$

$$RMSE^* = \frac{RMSE}{\sigma} \quad (4)$$

$$CC = \frac{\sum_{i=1}^{n}(y_i - \overline{y})(x_i - \overline{x})}{\sqrt{\sum_{i=1}^{n}(y_i - \overline{y})^2}\sqrt{(x_i - \overline{x})^2}} \quad (5)$$

$$NSE = 1 - \frac{\sum_{i=1}^{n}(y_i - x_i)^2}{(x_i - \overline{x})^2} \quad (6)$$

where y and x represent the predicted and actual timeseries; $\overline{y}$ and $\overline{x}$ represent the average of y and x; n is the number of data used; and σ is the standard deviation of actual timeseries.

2.3.2. Groundwater Storage Estimation

GWS_{GRACE} timeseries were estimated, over the investigated area, using the complete TW_{GRACE} record, SMS, and SWS timeseries (since the study area gets negligible amounts of snow, the snowpack component was ignored in the process of groundwater estimation) using Equation (7):

$$GWS_{GRACE} = TWS_{GRACE} - SMS - SWS \quad (7)$$

The errors in GWS_{GRACE} were estimated using the following equation:

$$\delta_{GWS} = \sqrt{\delta_{TWS}^2 + \delta_{SMS}^2 + \delta_{SWS}^2} \quad (8)$$

where δ_{GWS}, δ_{GRACE}, δ_{SMS}, and δ_{SWS} are the errors associated with GWS_{GRACE}, TW_{GRACE}, SMS, and SWS, respectively.

The spatial trends in TWS_{GRACE}, SMS, SWS, and GWS_{GRACE} were calculated using the same method that was adopted for temporal trends. To analyze changes in the spatial distribution of GWS_{GRACE}, the TWS_{GRACE} and SMS data were resampled at $0.25^\circ \times 0.25^\circ$ spatial grid scale. The SWS trend was estimated for each reservoir/lake area and interpolated to $0.25^\circ \times 0.25^\circ$ grid area.

2.3.3. Validation of Groundwater Storage

Thiessen polygon and simple average approaches were used to calculate the GWS_{well} timeseries used to validate GWS_{GRACE} timeseries. In both approaches the specific yield (Sy) values by well were extracted from the TWDB groundwater availability models (GAM) as well as the available literature [68,91–95]. In the first approach, the Thiessen polygons were constructed for the study area to estimate the area weighted GWS_{well} timeseries using the following equation [96,97]:

$$GWS_{well} = \frac{\sum_i^n S_i W_i \Delta h_i}{\sum_i^n W_i} \quad (9)$$

where S_i is the Sy for each Thiessen polygon i, n is the total number of polygons, W_i is the area of each polygon, and Δh_i is the average change in groundwater level in each polygon.

In the second approach, the GWL_{well} anomaly was calculated for individual wells and then the average GWL_{well} timeseries was calculated for the entire study area. Then, the GWS_{well} was calculated using the following equation [98]:

$$GWS_{well} = Averaged\ GWL_{well} * Sy * Total\ Area \quad (10)$$

2.3.4. Trend Calculations and Error Analysis

Short- and long-term trends in the TWS_{GRACE} and GWS_{GRACE} were calculated to characterize spatiotemporal variabilities. First, the annual cycle was calculated and removed from each timeseries before calculating the trend. This step is necessary as extreme events (i.e., flooding and drought) can lead to abrupt changes in the TWS_{GRACE} that are not directly related to changes in the GWS. The trend in TWS_{GRACE} and GWS_{GRACE} was then calculated using the breakpoint detection algorithm described in detail in previous studies [38,99–101].

The TWS_{GRACE} timeseries errors and trend were calculated as described by Ahmed and Abdelmohsen [28]. Briefly, the timeseries was first fitted using annual, semi-annual, and trend terms, and the residuals were smoothed using a 13-month moving average and a second set of residuals was calculated. The error in monthly timeseries was calculated as a standard deviation of the second set of residuals. A Monte Carlo simulation approach was used to calculate the trend error [102,103]. This approach simulated multiple synthetic timeseries, each with a Gaussian-distributed population and a standard deviation similar to that of the second set of residuals. The standard deviation of the synthetic trends was assigned as an error in the TWS_{GRACE} trend. Leakage errors in SH data over the

study area was estimated to be less than 90% of the error bar calculated for the average TWS_{GRACE} timeseries.

3. Results

3.1. Terrestrial Water Storage Reconstruction Results

Overall, the ANN and MLR models show similar results and good performance in training, testing, and validation phases (Figure 3; Table 1). The ANN model shows better performance for the training and testing sets, while the MLR model performs best for the validation set (Table 1). Predicted TWS_{GRACE} data from both models are highly correlated with the actual TWS_{GRACE} for both testing and validation datasets (Figure 3b,c). Both models agree very well for the prediction of all TWS_{GRACE} data gaps (Figure 3d). The MLR model output was used to fill the TWS_{GRACE} data gaps and create a continuous data set since it outperformed the ANN model during the validation phase.

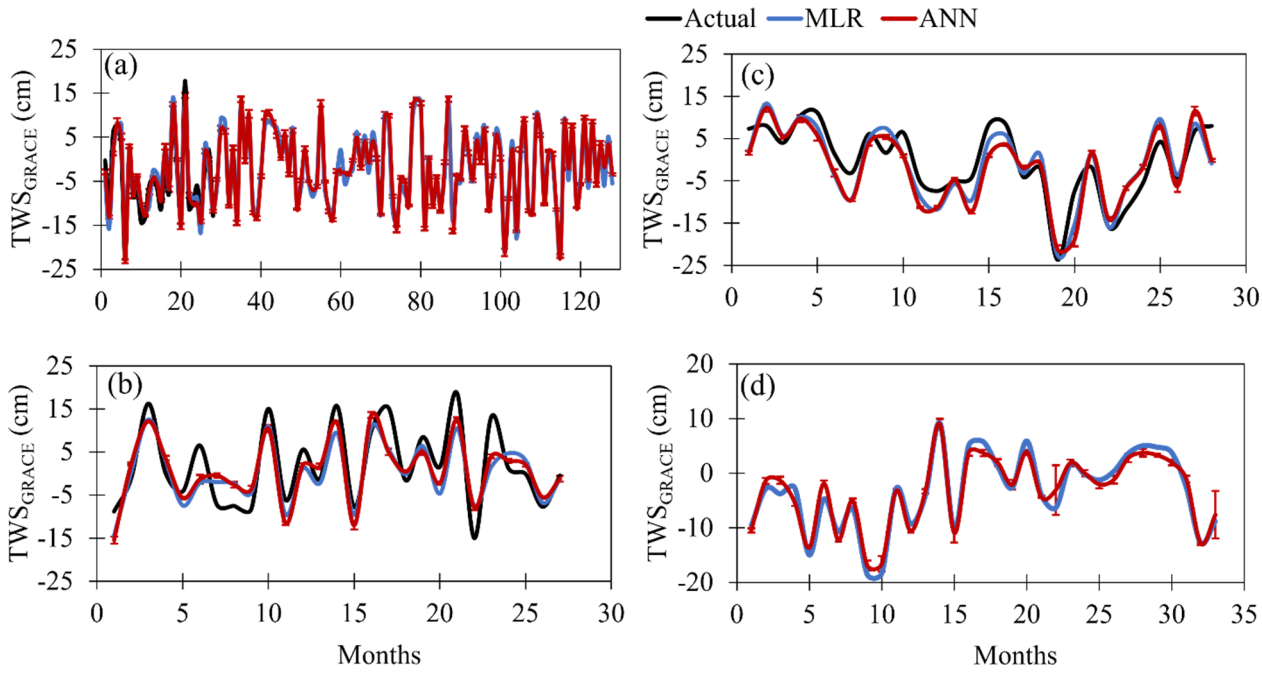

Figure 3. ANN (red) and MLR (black) model prediction results and associated model uncertainty for (**a**) training, (**b**) testing, (**c**) validation, and (**d**) prediction data. The "actual" observed data are represented by a black line. The error bars represent uncertainties in ANN model results calculated as standard deviation of 100 simulations.

Table 1. ANN and MLR model performance matrix.

	Model	RMSE	NRMSE	CC	NSE
Training	ANN	3.19	0.34	0.94	0.88
	MLR	3.79	0.57	0.92	0.83
Testing	ANN	5.00	0.53	0.88	0.71
	MLR	5.17	0.55	0.87	0.69
Validation	ANN	4.98	0.59	0.84	0.64
	MLR	4.29	0.51	0.85	0.73

3.2. Temporal Variation in Tresstrial Water Storage, Soil Moisture Storage, and Surface Water Storage

While we used the averaged TWS_{GRACE} solution generated from three SH and two mascon solutions, we also examined the agreements of the individual solutions (Figure 4a). Examination of temporal variations in TWS_{GRACE} shows that all five GRACE solutions

show a similar trend with slightly different amplitude during the investigated period (Figure 4a). The TWS_{GRACE} trends resulting from the CSR M, JPL M, GFZ SH, JPL SH, and CSR SH solutions are estimated to be -0.04 ± 0.07 km^3·yr^{-1} (p-value: 0.85), -0.04 ± 0.09 km^3·yr^{-1} (p-value: 0.87), -1.12 ± 0.09 km^3·yr^{-1} (p-value: <0.01), -0.54 ± 0.08 km^3·yr^{-1} (p-value: 0.02), -0.58 ± 0.08 km^3·yr^{-1} (p-value: 0.01), and -0.46 ± 0.08 km^3·yr^{-1} (p-value: 0.04), respectively.

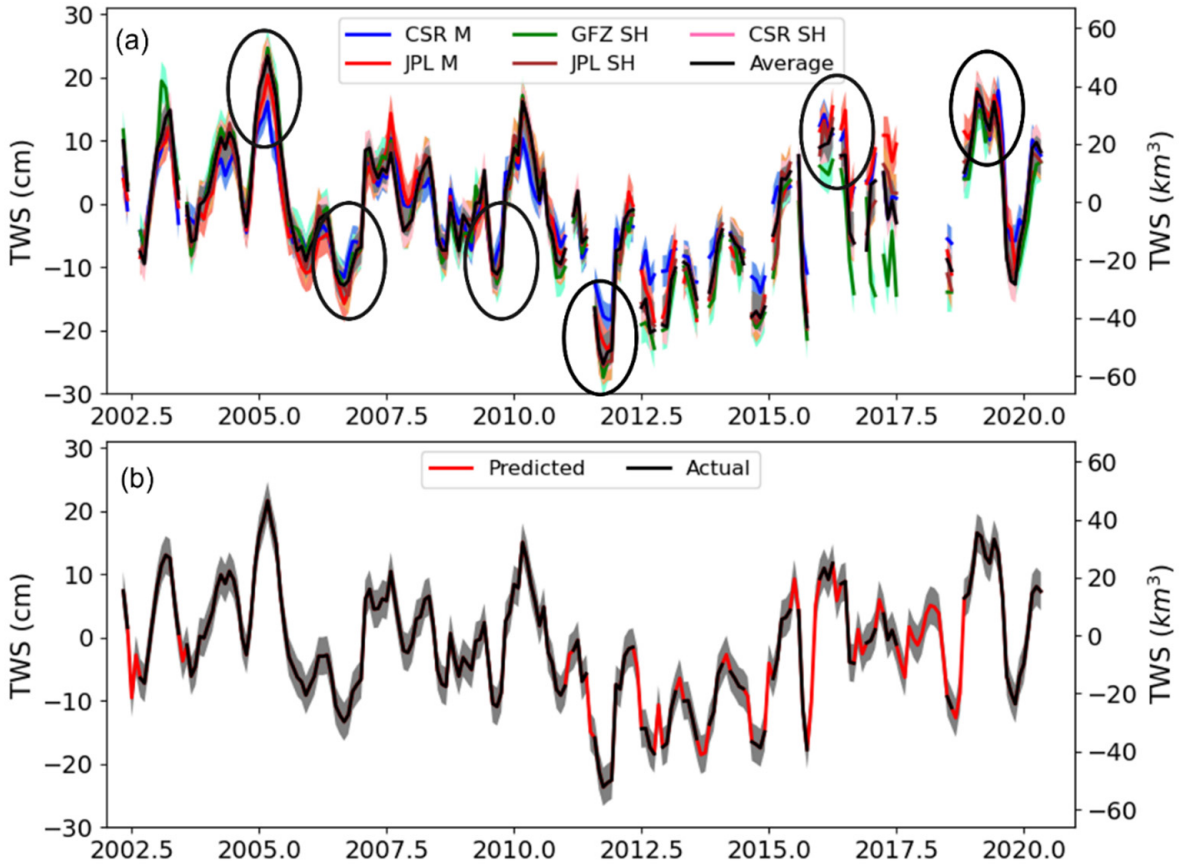

Figure 4. (**a**) Averages of temporal variations in JPL-SH, CSR-SH, GFZ-SH, JPL-M, CSR-M, and all solutions. (**b**) Complete TWS_{GRACE} timeseries after the data gaps ware filled with model predicted values. The black and red lines denote the actual and "predicted" values, respectively. The shaded regions represent errors of the respective timeseries. Extreme wet and dry periods are marked by the black ellipses.

All GRACE solutions captured very well the extreme hydroclimatic events (i.e., extreme wet and drought periods) that impacted the coastal area (Figure 4a). For instance, for the investigated period, there were three multi-year drought events (e.g., 2005–2006, 2007–2009, and 2010–2015). The lowest TWS_{GRACE} reached during the 2005–2006 and 2007–2009 droughts was estimated to be -29.35 km^3 and -24 km^3, respectively. All solutions show the maximum decline in TWS_{GRACE} after mid-2011 (average storage: -52.02 km^3), in September 2011, the driest year on record [104] (Figure 4a,b). The highest TWS_{GRACE} occurred at the beginning of 2005 following two hurricanes (Javier and Ivan) and one tropical storm (Matthew) that hit the Texas coastal region in fall 2004 [105]. Other extreme wet events are also captured in the TWS_{GRACE}, including the 2015 heavy rain and flooding (that ended the 2010–2015 drought), the 2016 severe weather and flooding, the 2018 south Texas heavy rain and flooding and the 2019 Tropical Depression Imelda.

No obvious seasonal changes in the TWS_{GRACE} were observed (Figure 4b), which is contrary to other studies that suggest distinct seasonality in TWS_{GRACE} in many basins across the world, with highs in winter and lows in summer [38,106]. Long et al. [83] noted

that the peak precipitation in Texas during spring and fall and low winter precipitation causes the absence of such distinct seasonal cycle in TWS_{GRACE}. For the Texas coastal area, a decreasing trend in TWS_{GRACE} is estimated from the complete timeseries at a rate of -0.43 ± 0.18 km^3·yr^{-1} (-0.2 ± 0.08 cm·yr^{-1}) with a p-value 0.06 (Figure 4b). Spatially, the entire area experiences depletion or no change in TWS_{GRACE} (Figure 5a). The highest depletion rate in TWS_{GRACE} for the 2002–2019 period (-0.6 to -0.4 cm·yr^{-1}) peaks in the central area of the study area, south of San Antonio and Austin (Figure 5a), an area experiencing increasing water demand and declining groundwater levels, particularly beginning with 2011, the driest year on record. Minimum to no changes in the TWS_{GRACE} characterize the rest of the study area to the east and west of the central area.

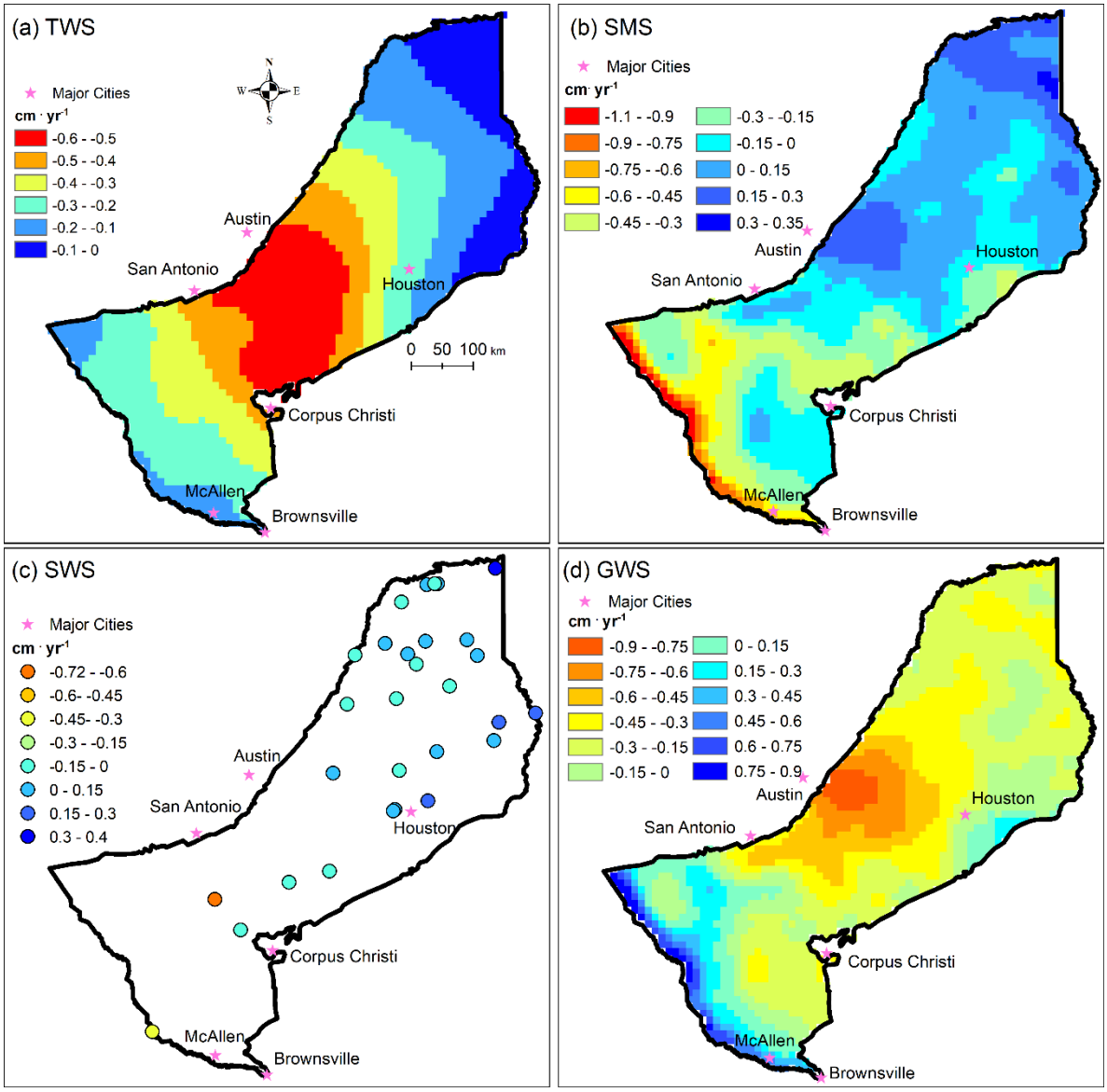

Figure 5. Spatial distribution of (**a**) TWS_{GRACE}, (**b**) SMS, (**c**) SWS, and (**d**) GWS_{GRACE} temporal trends. The cold colors in the figure represent an increasing (positive) trend and warm colors represent decreasing (negative) trends. The TWS_{GRACE}, SMS, and GWS_{GRACE} maps were interpolated to a $0.1^\circ \times 0.1^\circ$ grid scale.

The SMS and SWS timeseries show large monthly variations (Figure 6a,b) that generally follow the TWS_{GRACE} patterns (Figure 4). However, there is a notable difference between SMS extracted from different LSMs and those extracted from different versions

within the same model, especially during the extreme hydroclimatic periods. The observed variations between LSMs are attributed to the use of different forcing data, model parameters, and model structures [83]. The highest variability in SMS is associated with the NLDAS-Noah and GLDAS-Noah models, and the lowest with the VIC model, particularly during the extreme hydroclimatic time periods. Overall, average SMS declines significantly during the 2010–2015 drought period, with the most negative change in 2011 (-27.35 km^3), the driest year on record. During the 2005–2006 and 2007–2009 droughts, the lowest SMS storage was estimated at -7.2 km^3 and -23.2 km^3, respectively. The highest SMS storage was observed in 2005 and 2019 due to heavy rain and flooding, similar to the TWS_{GRACE} (see Section 3.1). For the duration of the record, average SMS decreases at a rate of -0.09 ± 0.13 km^3·yr^{-1} (0.04 ± 0.06 cm·yr^{-1}). Temporal variations in SWS are similar in trend to the TWS_{GRACE} and SMS. The lowest SWS (-5.48 km^3) was also observed during the most extreme drought year (i.e., 2011) and it decreases at a rate of -0.002 ± 0.01 km^3·yr^{-1} (0.004 ± 0.02 cm·yr^{-1}) over the study period.

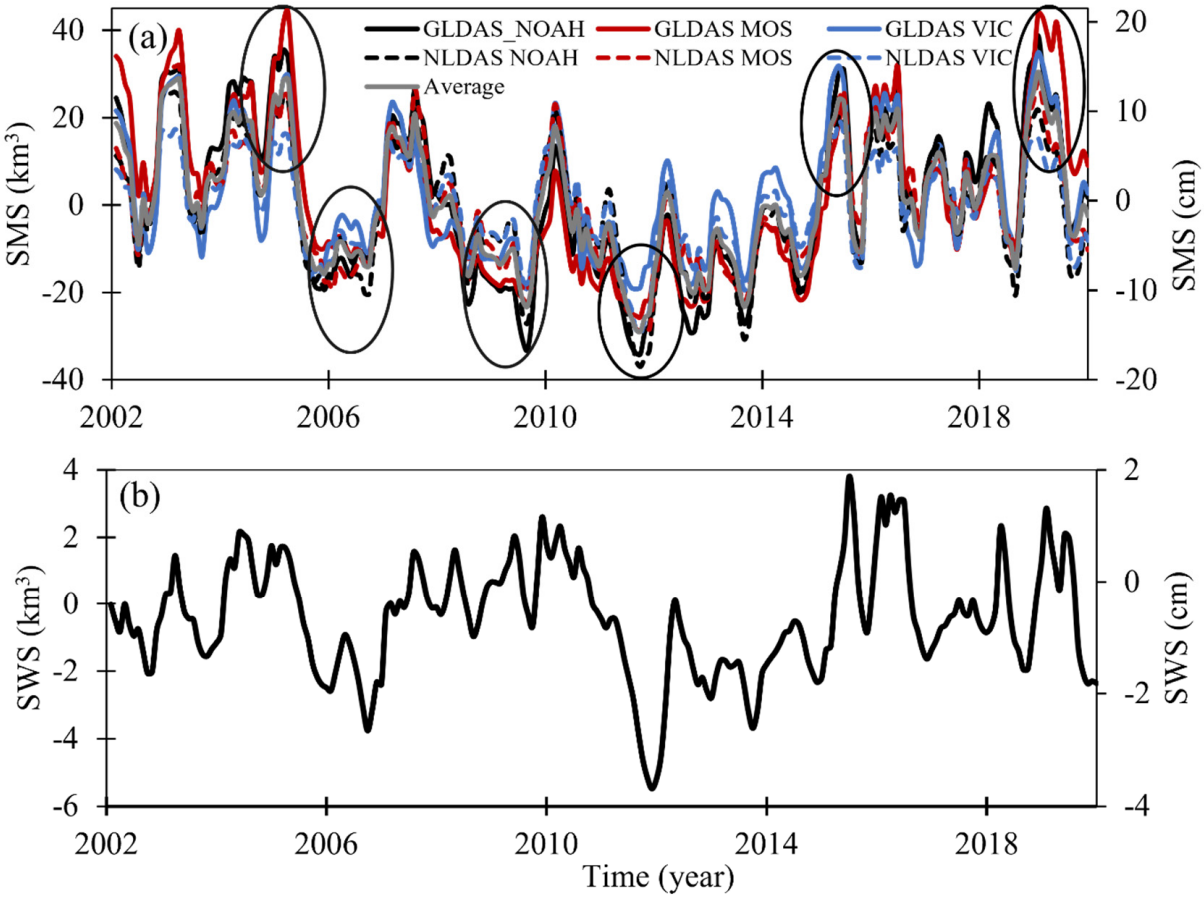

Figure 6. Temporal variations in (**a**) SMS and (**b**) SWS averaged over the study area. The black ellipses denote extreme wet and dry events.

Spatially, the SMS closely follows the climatic gradient (Figure 1c). An overwhelming majority of minimum to largest increases in SMS are characteristic of the northern half of the study area and to the east (0.35 to 0.15 cm·yr^{-1}), where the highest precipitation depths are observed. The highest depletion rates occur in the western half of the study area (Figure 5b), where precipitation rates are about twofold lower than to the east, while evaporation rates are greatest. Surface water reservoirs are mainly concentrated in the northeast half of the area, with 24 out of 29 reservoirs (Figure 5c) showing no change or an increase in the SWS over the study period. As with SMS, the largest increases in the SWS occur to the east (0.4 to 0.1 cm·yr^{-1}), including the greater Houston area. While

very limited in number, two out of five reservoirs located in the western half of the area experience the largest depletion rates in the SWS (-0.71 to -0.3 cm·yr^{-1}).

3.3. Temporal Variations in Groundwater Storage

Trend analyses indicate that the Texas coastal region experienced an overall decline in GWS_{GRACE} at -0.35 ± 0.08 km^3·yr^{-1} (0.15 ± 0.04 cm·yr^{-1}) (p-value < 0.01) for the investigated period, with large month-to-month variations (Figure 7). The lowest aquifer storage (-28.07 km^3) was observed immediately after the end of the longest drought (i.e., in September 2015) (Figure 7). During the 2005–2006 drought event, the aquifer storage reached a low of -14 km^3. Similar to the other storage compartments discussed above, the highest groundwater storage (i.e., 17 km^3) occurred in 2005, following downpours from tropical storms. During the 2007–2009 drought, the lowest storage was estimated at -7.4 km^3.

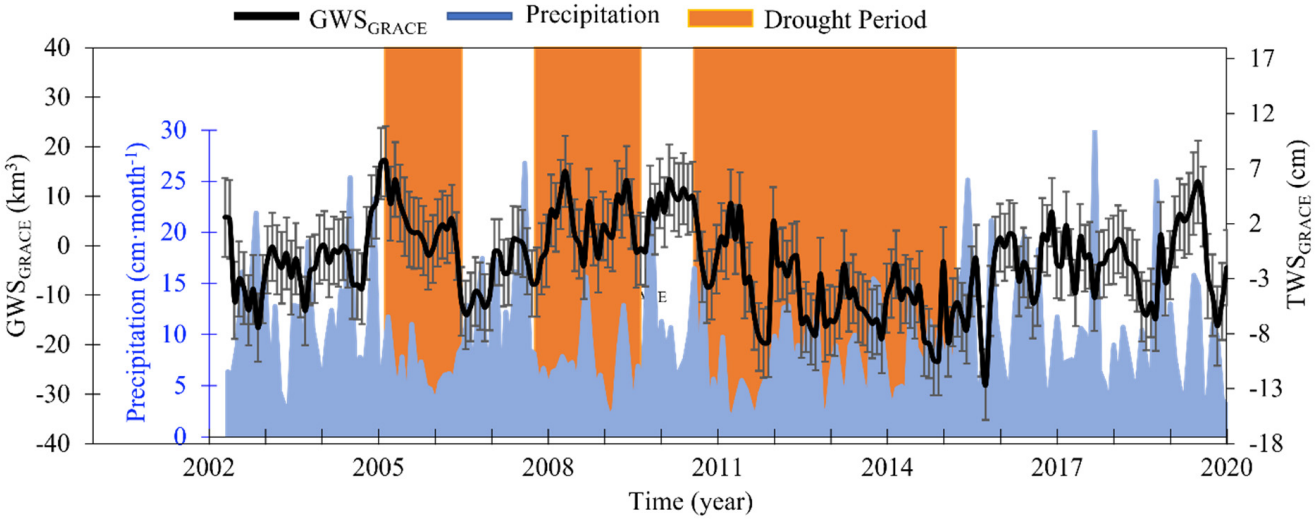

Figure 7. Temporal variation in GWS_{GRACE}. The blue bar graph represents the monthly precipitation, and the Texas drought periods are represented by vertical orange boxes.

The most significant decline in the GWS_{GRACE} occurred during the prolonged 2010–2015 drought period with a rate of -3.38 ± 0.43 km^3·yr^{-1} (1.54 ± 0.2 cm·yr^{-1}). However, a very small declining trend in TWS_{GRACE} (-0.1 ± 0.9 km^3·yr^{-1}) was observed over the entire drought period. It is expected that the difference in GWS_{GRACE} and TWS_{GRACE} trends is due to a quick response in SMS and SWS following the precipitation events that ended the drought and initiated the groundwater recharge. Conversely, the similar TWS_{GRACE} and GWS_{GRACE} response to drought is explained by depletion in SMS accompanied by an increase in groundwater extraction as the SWS resource was depleted (from 0.75 km^3 to -5.5 km^3) by drought and excessive use.

Inspection of the GWS_{GRACE} spatial trends (Figure 5d) shows an overall decreasing trend, except along the western border of the study region. This is the opposite to the SMS trend that shows the largest depletion rate in this region (Figure 5b). As with the TWS_{GRACE}, the largest depletion rate of the GWS_{GRACE} is in the central coastal region (-0.9 to -0.45 cm·yr^{-1}), an area where the change in SMS is minimum to none during the investigated period. Thus, the depletion in groundwater storage is captured with accuracy in the TWS_{GRACE} in this area.

3.4. Validation of GWS_{GRACE}

The GWL_{well} data has been used by a handful of studies to analyze changes in GWS and/or to validate GWS_{GRACE} [33,96,97,107]. In this study, the estimated GWS_{well} was used to validate the GWS_{GRACE} timeseries over the study area. The GWS_{well} from both Thiessen polygon and general average approaches show an overall significant increasing

trend (4.6 ± 0.19 km^3·yr^{-1} and 2.23 ± 0.14 km^3·yr^{-1}, respectively; with p-value < 0.01) for the 2011–2019 period (Figure 8). Comparatively, the GWS_{GRACE} also shows an increasing trend, but at a lower rate (1.05 ± 0.22 km^3·yr^{-1}, Figure 8).

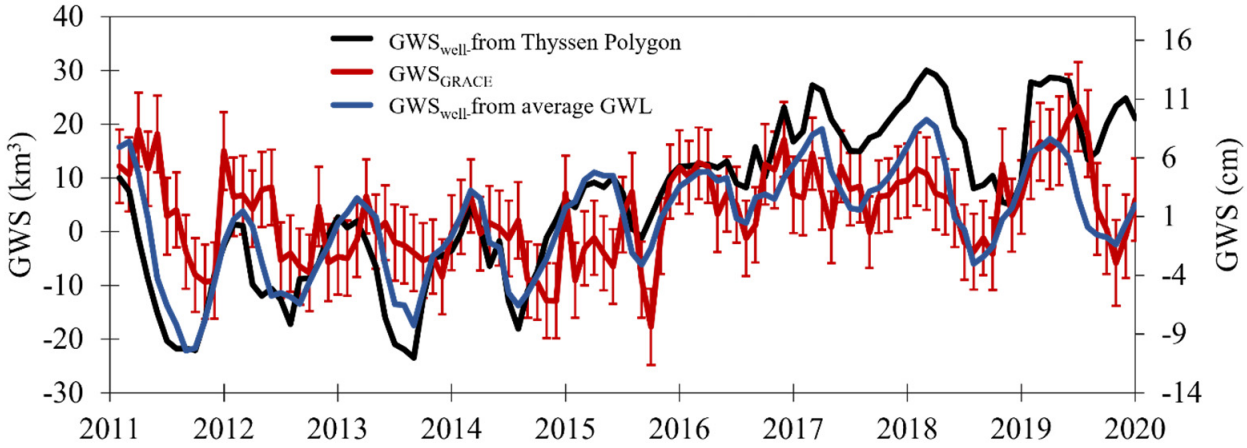

Figure 8. Estimated GWS_{well} from Thiessen polygon approach (black), general average approach (blue), and TWS_{GRACE} (red). Since most comprehensive GWL_{well} records are available beginning with 2012, the time mean of 2012–2016 was removed before GWS calculation.

The major differences in trend, and the time of the lowest storage peaks, between GWS_{GRACE} and GWS_{well}, occur during the drought period (i.e., 2010–2015). The lowest GWS_{well} using the Thiessen polygon and the general average methods is observed in 2011 (coinciding with the dip seen in the TWS_{GRACE}) and 2013, respectively. Comparatively the GWS_{GRACE} drops at the end of the drought period, in 2015. These differences may arise from the lack of even distribution of the groundwater level monitoring locations within the study area. Most of the groundwater monitoring stations are located in the central part of the region and only a few in the eastern and western parts, potentially leading to more bias in the estimated GWS_{well} towards conditions in the area with more coverage (e.g., central area). Additionally, in the absence of measured/calculated *Sy* data throughout the investigated area, the use of modelled *Sy* may also lead to larger uncertainties in the estimated GWS_{well}. Further discussions that aid explaining these discrepancies between different estimates of GWS are included in the discussion section. Regardless of slight discrepancies between the two records, there is a significant positive correlation between the GWS_{GRACE} and GWS_{well} (CC = 0.48; p-value < 0.01) generated from the Thiessen polygon approach. Additionally, a stronger correlation was observed between the GWS_{GRACE} and GWS_{well} records (CC = 0.56, p-value < 0.01) using the general average approach.

3.5. TWS_{GRACE} and GWS_{GRACE} Temporal Trend Analysis

The overall long-term TWS_{GRACE} trend is not statistically significant (trend: −0.43 ± 0.18 km^3·yr^{-1}; p-value: 0.06). However, there are short-term wet and dry periods throughout the investigated timeseries record with significant wetting and depletion trends. This is important to recognize since short-term variations in TWS_{GRACE} and GWS_{GRACE} could affect the groundwater management plans. Four short-term periods are revealed by the piecewise trend analysis of TWS_{GRACE} timeseries (Figure 9a, Table 2): Periods 1 (4/2002–5/2005) and 2 (6/2005–10/2010) show a significant TWS_{GRACE} wetting trend (7.73 ± 1.5 km^3·yr^{-1} and 2.96 ± 1 km^3·yr^{-1}; p-value < 0.01); and periods 3 (11/2010–2/2015) and 4 (3/2015–12/2019) show no significant trend (0.74 ± 0.84 km^3·yr^{-1}; p-value: 0.40 and 0.61 ± 1.3 km^3·yr^{-1}; p-value = 0.64).

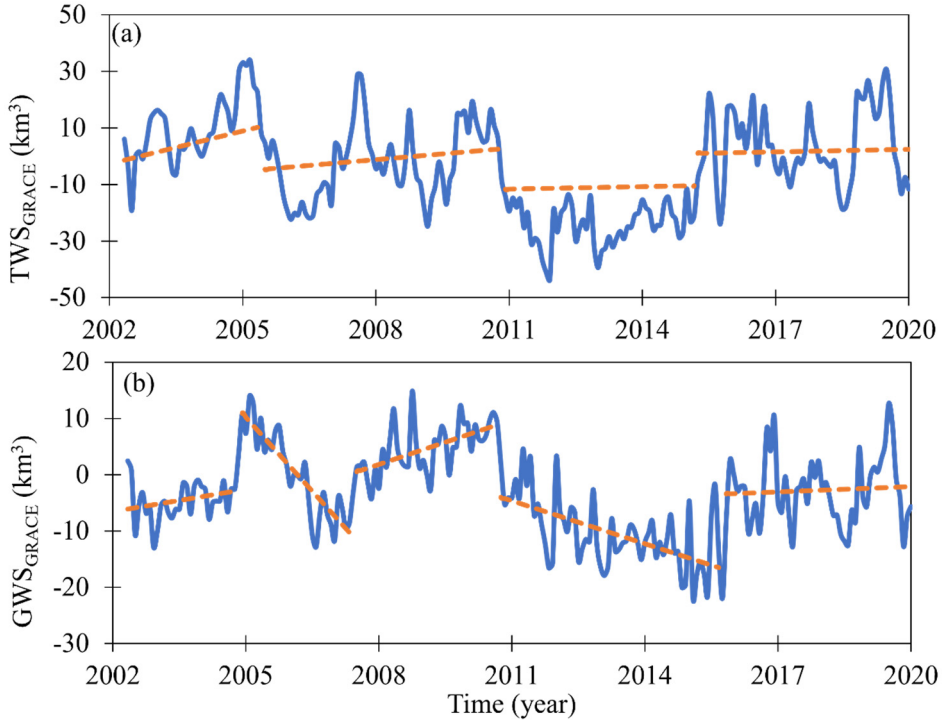

Figure 9. Temporal variations in de-seasoned/de-trended (**a**) TWS_{GRACE} and (**b**) GWS_{GRACE} time-series. Brown lines represent trend segments derived using the breakpoint detection algorithm.

Table 2. Piecewise analysis of trends in TWS_{GRACE} and GWS_{GRACE} over the Texas coastal aquifers.

Variables	Parameters	Period 1	Period 2	Period 3	Period 4	Period 5	Entire Period
TWS	Periods	4/2002–5/2005	6/2005–10/2010	11/2010–2/2015	3/2015–12/2019	–	4/2002–6/2019
	Trend ($km^3 \cdot yr^{-1}$)	7.73 ± 1.5	2.96 ± 1	0.74 ± 0.84	0.61 ± 1.3	–	-0.43 ± 0.18
	p-value	<0.01	<0.01	0.40	0.64	–	0.06
GWS	Periods	4/2002–10/2004	11/2004–5/2007	6/2007–8/2010	9/2010–9/2015	10/2015–12/2019	4/2002–6/2019
	Trend ($km^3 \cdot yr^{-1}$)	1.39 ± 0.71	-8.9 ± 0.95	2.6 ± 0.63	-2.67 ± 0.44	0.27 ± 0.74	-0.35 ± 0.078
	p-value	0.18	<0.01	<0.01	<0.01	0.70	<0.01

For the GWS_{GRACE}, trend analyses also reveal five short-term periods that are distinct from those of the TWS_{GRACE} timeseries. The record begins with a weak wetting trend, period 1 (14/2002–10/2004; 1.39 ± 0.71 $km^3 \cdot yr^{-1}$; *p*-value: 0.18), followed by period 2 (11/2004–5/2007), a strong drying trend (-8.9 ± 0.95 $km^3 \cdot yr^{-1}$; *p*-value < 0.01), period 3 (6/2007–8/2010), which is a moderate wet period (2.6 ± 0.63 $km^3 \cdot yr^{-1}$; *p*-value $\leq$ 0.01), and period 4 (9/2010–9/2015), a significant dry or depletion trend (-2.67 ± 0.44 $km^3 \cdot yr^{-1}$; *p*-value: <0.01). The end of the record shows an insignificant increasing trend of the GWS_{GRACE} (period 5, trend: 0.27 ± 0.74 $km^3 \cdot yr^{-1}$; *p*-value: 0.7; period 5: 10/2015–12/2019).

4. Discussion and Conclusions

The short-term changes in TWS_{GRACE} and GWS_{GRACE} trends observed in this study are attributed mainly to climatic variabilities, which when compounded by anthropogenic stressors result in different response times in the storage compartments. Overall, the TWS_{GRACE} shows an increasing tendency, while the GWS_{GRACE} experiences multiple increasing and decreasing trends. These discrepancies are mainly due to the different response time to precipitation and evapotranspiration of the two types of storages. For instance, precipitation and evapotranspiration are the main driver of TWS changes in low latitudes [108,109], particularly because of the relatively quick response of SMS to climatic factors. To exemplify this, in this study the lowest TWS_{GRACE} (-26.87 km^3) was observed

during the peak of the extreme drought (i.e., 2011) (Figure 10) with the lowest total annual precipitation (57.2 cm; Figure 10) that represented only 55% of the average total annual precipitation observed during the investigation period (103.9 cm).

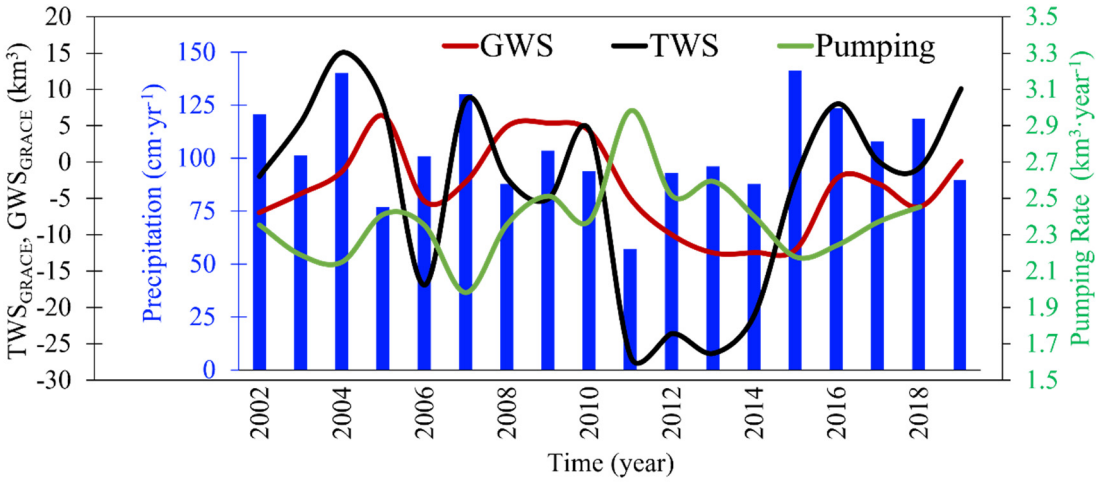

Figure 10. Annual averaged TWS_{GRACE} (black), GWS_{GRACE} (red), and groundwater pumping rate (green). The annual precipitation is presented (blue) as vertical bars.

While highly dependent on the region's hydrogeologic characteristics (i.e., aquifer permeabilities) and water use practices (i.e., groundwater extraction for irrigation and/or human consumption), GWS is expected to have a delayed response to changing climatic conditions. The highest groundwater extraction rate (3 $km^3 \cdot yr^{-1}$; Figure 10) for the study period occurred in the driest year on record (e.g., 2011), likely a result of increased groundwater usage for irrigation as precipitation amounts and surface water resources have been steadily declining since the beginning of the drought period in 2010. Nonetheless, the lowest annual average GWS_{GRACE} (−12 km^3) was observed at the end of the prolonged drought, in 2015 (Figure 10). The effects of groundwater abstractions on groundwater storage are not always straightforward and are a function of time following the initiation of stress [110] and the density of pumping wells. Initial stages of pumping cause a quick depletion in storage (e.g., year 2011 in this study), as a cone of depression forms to fulfill the pumping volumes [111]. In an area with dense network of pumping wells (e.g., the greater Houston area; Figure 1b), prolonged pumping may cause cones of depression to fuse with each other; thus, further pumping will result in an overall depletion of the area. If pumping rates remain fairly constant, an equilibrium is generally achieved as time progresses, and the change in the cone of depression and GWS is very small concerning its observation by GRACE.

During prolonged drought periods, pumping likely exceeds natural recharge, thus violating the quasi-equilibrium condition of the cone of depression. Rather, dewatering of the aquifer increases with time in the near vicinity of pumping, thus the lower GWS_{GRACE} years after the most severe precipitation drought. Thus, GWS_{GRACE} captures responses linked to climate-induced groundwater depletion.

Some areas within the Texas coastal region have had groundwater elevations substantially below sea level throughout the investigated period. For example, Jasechko et al. [17] found that 25% of the groundwater elevations within 10 km of the coast in the GCA are below sea level. Within the greater Houston area, average groundwater elevations from nine wells ranged between 30 m (early 2011) and 35 m (late 2011–early 2012) below mean sea level between 2011 and 2020. This confirms that changes in GWS in certain areas may not be significant if aquifer depletion has occurred before the beginning of this study's record.

Groundwater elevations below mean sea level are an indication that sea water intrusion may have occurred and, given the hydrogeologic makeup of the area (e.g., fine sand and clay formations with low permeabilities) and the observed land subsidence (i.e., the

Greater Houston area and other areas along the coast) [20], changes in these conditions are expected to be insignificant over the duration of the study [112,113]. However, storage depletion in other areas that have not been historically impacted by overproduction of aquifers (e.g., the central portion of the study area where groundwater elevations fluctuate between 34 m (late 2011) and 42 m (mid 2019) above mean sea level between 2011 and 2020) is expected to be captured within the study time frame. In systems like this, accelerated aquifer depletion is expected, particularly in periods of prolonged drought when the stress on groundwater is initiated in the early stages and increases over time with equilibrium likely attained in the later stages of the drought. In consequence, these systems are likely to weigh more significantly into the observed GWS_{GRACE} changes. Additional research on the spatial changes of GWS in areas affected by sea water intrusion versus those that are impacted during drought conditions, like a regional groundwater flow and transport model, is necessary to further understand how GWS_{GRACE} may be impacted.

Author Contributions: Conceptualization, B.G. and D.M.; methodology, B.G., D.M. and M.A.; software, B.G.; validation, B.G., D.M. and M.A.; formal analysis, investigation, resources, and data curation, B.G., D.M. and M.A.; writing—original draft preparation, B.G.; writing—review and editing, B.G., D.M. and M.A.; visualization, B.G.; supervision, D.M. and M.A.; project administration, B.G. and D.M.; funding acquisition, B.G. and D.M. All authors have read and agreed to the published version of the manuscript.

Funding: This work was supported in part by an Institutional Grant (NA14OAR4170102) to the Texas Sea Grant College Program from the National Sea Grant Office, National Oceanic and Atmospheric Administration, U.S. Department of Commerce, and an Institutional Grant to the Texas General Office, Coastal Management Program pursuant to National Oceanic and Atmospheric Administration award (NA13NOS4190113).

Informed Consent Statement: Not Applicable.

Data Availability Statement: Not applicable.

Acknowledgments: Texas Sea Grant GIAR and the Center for Water Supply Studies and the Center for Water Supply Studies and Department of Physical and Environmental Sciences at Texas A & M University-Corpus Christi (TAMU-CC) financially supported this research and ARD's dissertation from which this paper has been derived. All views, opinions, findings, and conclusions presented herein are those of the authors and do not necessarily reflect the opinions of sponsors.

Conflicts of Interest: The authors declare no conflict of interest. The funders had no role in the design of the study; in the collection, analyses, or interpretation of data; in the writing of the manuscript, or in the decision to publish the results.

References

1. Alley, W.M.; Healy, R.W.; LaBaugh, J.W.; Reilly, T.E. Flow and Storage in Groundwater Systems. *Science* **2002**, *296*, 1985–1990. [CrossRef] [PubMed]
2. Smith, M.; Cross, K.; Paden, M.; Laban, P. *Spring–Managing Groundwater Sustainably*; IUCN: Gland, Switzerland, 2016.
3. Wada, Y.; Van Beek, L.P.H.; Van Kempen, C.M.; Reckman, J.W.T.M.; Vasak, S.; Bierkens, M.F.P. Global depletion of groundwater resources. *Geophys. Res. Lett.* **2010**, *37*, 37. [CrossRef]
4. Custodio, E.; Cabrera, M.D.; Poncela, R.; Puga, L.-O.; Skupien, E.; del Villar, A. Groundwater intensive exploitation and mining in gran Canaria and Tenerife, CanaryI, Spain: Hydrogeological, Environmental, Economic and social aspects. *Sci. Total Environ.* **2016**, *557*, 425–437. [CrossRef] [PubMed]
5. Ahmed, M.; Aqnouy, M.; El Messari, J.S. Sustainability of Morocco's groundwater resources in response to natural and anthropogenic forces. *J. Hydrol.* **2021**, *603*, 126866. [CrossRef]
6. Ahmed, M. Sustainable management scenarios for northern Africa's fossil aquifer systems. *J. Hydrol.* **2020**, *589*, 125196. [CrossRef]
7. Konikow, L.F. Contribution of global groundwater depletion since 1900 to sea-level rise. *Geophys. Res. Lett.* **2011**, *38*. [CrossRef]
8. Konikow, L.F. Long-Term Groundwater Depletion in the United States. *Ground Water* **2014**, *53*, 2–9. [CrossRef]
9. Small, C.; Nicholls, R.J. A global analysis of human settlement in coastal zones. *J. Coast. Res.* **2003**, *19*, 584–599.
10. Post, V. Fresh and saline groundwater interaction in coastal aquifers: Is our technology ready for the problems ahead? *Hydrogeol. J.* **2005**, *13*, 120–123. [CrossRef]
11. Gaaloul, N.; Pliakas, F.; Kallioras, A.; Schuth, C.; Marinos, P. Simulation of seawater intrusion in coastal aquifers: Forty five-years exploitation in an eastern coast aquifer in Tunisia. *Open Hydrol. J.* **2012**, *6*, 31–44. [CrossRef]

12. Jasechko, S.; Perrone, D.; Seybold, H.; Fan, Y.; Kirchner, J.W. Groundwater level observations in 250,000 coastal US wells reveal scope of potential seawater intrusion. *Nat. Commun.* **2020**, *11*, 3229. [CrossRef] [PubMed]
13. Werner, A.D.; Simmons, C.T. Impact of Sea-Level Rise on Sea Water Intrusion in Coastal Aquifers. *Groundwater* **2009**, *47*, 197–204. [CrossRef] [PubMed]
14. Chinnasamy, P.; Sunde, M.G. Improving spatiotemporal groundwater estimates after natural disasters using remotely sensed data–a case study of the Indian Ocean tsunami. *Earth Sci. Inform.* **2016**, *9*, 101–111. [CrossRef]
15. Murgulet, D.; Tick, G. The extent of saltwater intrusion in southern Baldwin County, Alabama. *Environ. Geol.* **2008**, *55*, 1235–1245. [CrossRef]
16. Niyazi, B.A.; Ahmed, M.; Basahi, J.M.; Masoud, M.Z.; Rashed, M.A. Spatiotemporal trends in freshwater availability in the Red Sea Hills, Saudi Arabia. *Arab. J. Geosci.* **2018**, *11*, 702. [CrossRef]
17. Famiglietti, J.; Lo, M.; Ho, S.; Bethune, J.; Anderson, K.; Syed, T.; Swenson, S.; de Linage, C.; Rodell, M. Satellites measure recent rates of groundwater depletion in California's Central Valley. *Geophys. Res. Lett.* **2011**, *38*, L03403. [CrossRef]
18. Niyazi, B.A.; Ahmed, M.; Masoud, M.Z.; Rashed, M.A.; Basahi, J.M. Sustainable and resilient management scenarios for groundwater resources of the Red Sea coastal aquifers. *Sci. Total Environ.* **2019**, *690*, 1310–1320. [CrossRef]
19. Ferguson, G.; Gleeson, T. Vulnerability of coastal aquifers to groundwater use and climate change. *Nat. Clim. Chang.* **2012**, *2*, 342–345. [CrossRef]
20. Haley, M.; Ahmed, M.; Gebermichael, E.; Murgulet, D.; Starek, M. Land Subsidence in the Texas Coastal Bend: Locations, Rates, Triggers, and Consequences. *Remote Sens.* **2022**, *14*, 192. [CrossRef]
21. Seneviratne, S.; Viterbo, P.; Lüthi, D.; Schär, C. Inferring Changes in Terrestrial Water Storage Using ERA-40 Reanalysis Data: The Mississippi River Basin. *J. Clim.* **2004**, *17*, 2039–2057. [CrossRef]
22. Rodell, M.; Famiglietti, J. An analysis of terrestrial water storage variations in Illinois with implications for the Gravity Recovery and Climate Experiment (GRACE). *Water Resour. Res.* **2001**, *37*, 1327–1339. [CrossRef]
23. Mogheir, Y.; De Lima, J.L.M.P.; Singh, V.P. Assessment of Informativeness of Groundwater Monitoring in Developing Regions (Gaza Strip Case Study). *Water Resour. Manag.* **2005**, *19*, 737–757. [CrossRef]
24. Shah, T.; Molden, D.; Sakthivadivel, R.; Seckler, D. *Groundwater: Overview of Opportunities and Challenges*; IWMI: Colombo, Sri Lanka, 2000.
25. Taylor, C.J.; Alley, W.M. *Ground-Water-Level Monitoring and the Importance of Long-Term Water-Level Data*; US Geological Survey: Denver, CO, USA, 2002.
26. Tuinhof, A.; Foster, S.; Kemper, K.; Garduno, H.; Nanni, M. *Groundwater Monitoring Requirements for Managing Aquifer Response and Quality Threats*; World Bank Briefing Note 9; World Bank: Washington, DC, USA, 2003.
27. Fallatah, O.A.; Ahmed, M.; Save, H.; Akanda, A.S. Quantifying temporal variations in water resources of a vulnerable middle eastern transboundary aquifer system. *Hydrol. Process.* **2017**, *31*, 4081–4091. [CrossRef]
28. Ahmed, M.; Abdelmohsen, K. Quantifying Modern Recharge and Depletion Rates of the Nubian Aquifer in Egypt. *Surv. Geophys.* **2018**, *39*, 729–751. [CrossRef]
29. Fallatah, O.A.; Ahmed, M.; Cardace, D.; Boving, T.; Akanda, A.S. Assessment of modern recharge to arid region aquifers using an integrated geophysical, geochemical, and remote sensing approach. *J. Hydrol.* **2019**, *569*, 600–611. [CrossRef]
30. Tapley, B.D.; Bettadpur, S.; Watkins, M.; Reigber, C. The gravity recovery and climate experiment: Mission overview and early results. *Geophys. Res. Lett.* **2004**, *31*, L09607. [CrossRef]
31. Landerer, F.W.; Flechtner, F.M.; Save, H.; Webb, F.H.; Bandikova, T.; Bertiger, W.I.; Bettadpur, S.V.; Byun, S.H.; Dahle, C.; Dobslaw, H.; et al. Extending the Global Mass Change Data Record: GRACE Follow-On Instrument and Science Data Performance. *Geophys. Res. Lett.* **2020**, *47*. [CrossRef]
32. Voss, K.A.; Famiglietti, J.S.; Lo, M.-H.; De Linage, C.; Rodell, M.; Swenson, S.C. Groundwater depletion in the Middle East from GRACE with implications for transboundary water management in the Tigris-Euphrates-Western Iran region. *Water Resour. Res.* **2013**, *49*, 904–914. [CrossRef]
33. Rodell, M.; Chen, J.S.; Kato, H.; Famiglietti, J.; Nigro, J.; Wilson, C.R. Estimating groundwater storage changes in the Mississippi River basin (USA) using GRACE. *Hydrogeol. J.* **2006**, *15*, 159–166. [CrossRef]
34. Rodell, M.; Velicogna, I.; Famiglietti, J.S. Satellite-based estimates of groundwater depletion in India. *Nature* **2009**, *460*, 999–1002. [CrossRef]
35. Mohamed, A.; Sultan, M.; Ahmed, M.; Yan, E.; Ahmed, E. Aquifer recharge, depletion, and connectivity: Inferences from GRACE, land surface models, and geochemical and geophysical data. *Bulletin* **2017**, *129*, 534–546. [CrossRef]
36. Ahmed, M.; Sultan, M.; Wahr, J.; Yan, E. The use of GRACE data to monitor natural and anthropogenic induced variations in water availability across Africa. *Earth-Sci. Rev.* **2014**, *136*, 289–300. [CrossRef]
37. Ahmed, M.; Sultan, M.; Wahr, J.; Yan, E.; Milewski, A.; Sauck, W.; Becker, R.; Welton, B. Integration of GRACE (Gravity Recovery and Climate Experiment) data with traditional data sets for a better understanding of the time-dependent water partitioning in African watersheds. *Geology* **2011**, *39*, 479–482. [CrossRef]
38. Ahmed, M.; Wiese, D.N. Short-term trends in Africa's freshwater resources: Rates and drivers. *Sci. Total Environ.* **2019**, *695*, 133843. [CrossRef] [PubMed]
39. Xenarios, S.; Schmidt-Vogt, D.; Qadir, M.; Janusz-Pawletta, B.; Abdullaev, I. *The Aral Sea Basin: Water for Sustainable Development in Central Asia*; Routledge: London, UK, 2019.

40. Feng, W.; Zhong, M.; Lemoine, J.-M.; Biancale, R.; Hsu, H.-T.; Xia, J. Evaluation of groundwater depletion in North China using the Gravity Recovery and Climate Experiment (GRACE) data and ground-based measurements. *Water Resour. Res.* **2013**, *49*, 2110–2118. [CrossRef]
41. Ebead, B.; Ahmed, M.; Niu, Z.; Huang, N. Quantifying the anthropogenic impact on groundwater resources of North China using Gravity Recovery and Climate Experiment data and land surface models. *J. Appl. Remote Sens.* **2017**, *11*, 26029. [CrossRef]
42. Shamsudduha, M.; Taylor, R.; Longuevergne, L. Monitoring groundwater storage changes in the highly seasonal humid tropics: Validation of GRACE measurements in the Bengal Basin. *Water Resour. Res.* **2012**, *48*. [CrossRef]
43. Ahmed, M.; Sultan, M.; Elbayoumi, T.; Tissot, P. Forecasting GRACE Data over the African Watersheds Using Artificial Neural Networks. *Remote Sens.* **2019**, *11*, 1769. [CrossRef]
44. Yozgatligil, C.; Aslan, S.; Iyigun, C.; Batmaz, I. Comparison of missing value imputation methods in timeseries: The case of Turkish meteorological data. *Theor. Appl. Climatol.* **2013**, *112*, 143–167. [CrossRef]
45. Campozano, L.; Sánchez, E.; Avilés, Á.; Samaniego, E. Evaluation of infilling methods for timeseries of daily precipitation and temperature: The case of the Ecuadorian Andes. *Maskana* **2014**, *5*, 99–115. [CrossRef]
46. Gould, P.G.; Koehler, A.B.; Ord, J.K.; Snyder, R.; Hyndman, R.; Vahid-Araghi, F. Forecasting time series with multiple seasonal patterns. *Eur. J. Oper. Res.* **2008**, *191*, 207–222. [CrossRef]
47. Mwale, F.; Adeloye, A.; Rustum, R. Infilling of missing rainfall and streamflow data in the Shire River basin, Malawi—A self organizing map approach. *Phys. Chem. Earth Parts A/B/C* **2012**, *50–52*, 34–43. [CrossRef]
48. Bredow, E.; Steinberger, B. Variable Melt Production Rate of the Kerguelen HotSpot Due To Long-Term Plume-Ridge Interaction. *Geophys. Res. Lett.* **2018**, *45*, 126–136. [CrossRef]
49. Nie, W.; Zaitchik, B.F.; Rodell, M.; Kumar, S.V.; Arsenault, K.R.; Li, B.; Getirana, A. Assimilating GRACE Into a Land Surface Model in the Presence of an Irrigation-Induced Groundwater Trend. *Water Resour. Res.* **2019**, *55*, 11274–11294. [CrossRef]
50. Shokri, A.; Walker, J.; van Dijk, A.I.J.M.; Pauwels, V.R.N. Performance of Different Ensemble Kalman Filter Structures to Assimilate GRACE Terrestrial Water Storage Estimates Into a High-Resolution Hydrological Model: A Synthetic Study. *Water Resour. Res.* **2018**, *54*, 8931–8951. [CrossRef]
51. Sun, A.Y.; Scanlon, B.R.; Zhang, Z.; Walling, D.; Bhanja, S.N.; Mukherjee, A.; Zhong, Z. Combining physically based modeling and deep learning for fusing GRACE satellite data: Can we learn from mismatch? *Water Resour. Res.* **2019**, *55*, 1179–1195. [CrossRef]
52. Broxton, P.D.; Van Leeuwen, W.J.; Biederman, J.A. Improving Snow Water Equivalent Maps With Machine Learning of Snow Survey and Lidar Measurements. *Water Resour. Res.* **2019**, *55*, 3739–3757. [CrossRef]
53. Kim, D.; Yu, H.; Lee, H.; Beighley, E.; Durand, M.; Alsdorf, D.E.; Hwang, E. Ensemble learning regression for estimating river discharges using satellite altimetry data: Central Congo River as a Test-bed. *Remote Sens. Environ.* **2018**, *221*, 741–755. [CrossRef]
54. Tran, H.; Leonarduzzi, E.; de la Fuente, L.; Hull, R.B.; Bansal, V.; Chennault, C.; Gentine, P.; Melchior, P.; Condon, L.E.; Maxwell, R.M. Development of a deep learning emulator for a distributed groundwater–surface water model: Parflow-ml. *Water* **2021**, *13*, 3393. [CrossRef]
55. Feng, D.; Fang, K.; Shen, C. Enhancing Streamflow Forecast and Extracting Insights Using Long-Short Term Memory Networks With Data Integration at Continental Scales. *Water Resour. Res.* **2020**, *56*. [CrossRef]
56. Pan, B.; Hsu, K.; AghaKouchak, A.; Sorooshian, S. Improving Precipitation Estimation Using Convolutional Neural Network. *Water Resour. Res.* **2019**, *55*, 2301–2321. [CrossRef]
57. Sun, Z.; Long, D.; Yang, W.; Li, X.; Pan, Y. Reconstruction of GRACE Data on Changes in Total Water Storage Over the Global Land Surface and 60 Basins. *Water Resour. Res.* **2020**, *56*. [CrossRef]
58. Li, F.; Kusche, J.; Rietbroek, R.; Wang, Z.; Forootan, E.; Schulze, K.; Lück, C. Comparison of Data-Driven Techniques to Reconstruct (1992–2002) and Predict (2017–2018) GRACE-Like Gridded Total Water Storage Changes Using Climate Inputs. *Water Resour. Res.* **2020**, *56*, e2019WR026551. [CrossRef]
59. Yi, S.; Sneeuw, N. Filling the Data Gaps Within GRACE Missions Using Singular Spectrum Analysis. *J. Geophys. Res. Solid Earth* **2021**, *126*. [CrossRef]
60. Seo, J.Y.; Lee, S.-I. Spatio-Temporal Groundwater Drought Monitoring Using Multi-Satellite Data Based on an Artificial Neural Network. *Water* **2019**, *11*, 1953. [CrossRef]
61. Milewski, A.M.; Thomas, M.B.; Seyoum, W.M.; Rasmussen, T.C. Spatial Downscaling of GRACE TWSA Data to Identify Spatiotemporal Groundwater Level Trends in the Upper Floridan Aquifer, Georgia, USA. *Remote Sens.* **2019**, *11*, 2756. [CrossRef]
62. Jyolsna, P.J.; Kambhammettu, B.V.N.P.; Gorugantula, S. Application of random forest and multi-linear regression methods in downscaling GRACE derived groundwater storage changes. *Hydrol. Sci. J.* **2021**, *66*, 874–887. [CrossRef]
63. Malakar, P.; Mukherjee, A.; Bhanja, S.N.; Ray, R.K.; Sarkar, S.; Zahid, A. Machine-learning-based regional-scale groundwater level prediction using GRACE. *Hydrogeol. J.* **2021**, *29*, 1027–1042. [CrossRef]
64. TWDB. *TWDB, Texas Precipitation*; Texas Water Development Board: Austin, TX, USA, 2021.
65. U.S. Census Bureau. *2000 Census of Population and Housing*; U.S. Census Bureau: Washington, DC, USA, 2003.
66. Ashworth, J.B. Aquifer Summaries, Texas. In *Aquifers of Texas*; Texas Water Development Board: Austin, TX, USA, 1995.
67. Boghici, R. The Carrizo Wilcox aquifer of Texas: Groundwater chemistry, origin, and ages. *Gulf Coast Assoc. Geol. Soc. Trans.* **2008**, *58*, 105–123.
68. Chowdhury, A.H.; Wade, S.; Mace, R.E.; Ridgeway, C. *Groundwater Availability Model of the Central Gulf Coast Aquifer System: Numerical Simulations through 1999*; unpublished report 1; Texas Water Development Board: Austin, TX, USA, 2004; p.14.

69. Chowdhury, A.H.; Turco, M.J. Geology of the Gulf Coast aquifer, Texas. In *Aquifers of the Gulf Coast of Texas*; Texas Water Development Board: Austin, TX, USA, 2006.
70. Mace, R.E.; Smyth, R.C. *Hydraulic Properties of the Carrizo Wilcox Aquifer in Texas: Information for Groundwater Modeling, Planning, and Management*; Bureau of Economic Geology, University of Texas at Austin: Austin, TX, USA, 2003.
71. TWDB. *Water for Texas 2012 State Water Plan*; Texas Water Development Board: Austin, TX, USA, 2012; pp. 144–155.
72. Thornthwaite, C.W. An approach toward a rational classification of climate. *Geogr. Rev.* **1948**, *38*, 55–94. [CrossRef]
73. Landerer, F.W.; Swenson, S.C. Accuracy of scaled GRACE terrestrial water storage estimates. *Water Resour. Res.* **2012**, *48*, W04531. [CrossRef]
74. Wiese, D.; Yuan, D.; Boening, C.; Landerer, F.; Watkins, M. JPL GRACE Mascon Ocean, Ice, and Hydrology Equivalent Water Height Release 06 Coastal Resolution Improvement (Cri) FilTered Version 1.0; Ver, 2018. Available online: https://doi.org/10.5067/TEMSC-3MJC6 (accessed on 24 January 2022).
75. Save, H.; Bettadpur, S.; Tapley, B.D. High-resolution CSR GRACE Rl05 Mascons. *J. Geophys. Res. Solid Earth* **2016**, *121*, 7547–7569. [CrossRef]
76. Long, D.; Chen, X.; Scanlon, B.R.; Wada, Y.; Hong, Y.; Singh, V.P.; Chen, Y.; Wang, C.; Han, Z.; Yang, W. Have GRACE satellites overestimated groundwater depletion in the northwest India aquifer? *Sci. Rep.* **2016**, *6*, 24398. [CrossRef] [PubMed]
77. Sakumura, C.; Bettadpur, S.; Bruinsma, S. Ensemble prediction and intercomparison analysis of GRACE time-variable gravity field models. *Geophys. Res. Lett.* **2014**, *41*, 1389–1397. [CrossRef]
78. Rodell, M.; Houser, P.R.; Jambor, U.; Gottschalck, J.; Mitchell, K.; Meng, C.-J.; Arsenault, K.; Cosgrove, B.; Radakovich, J.; Bosilovich, M.; et al. The Global Land Data Assimilation System. *Bull. Am. Meteorol. Soc.* **2004**, *85*, 381–394. [CrossRef]
79. Xia, Y.; Mitchell, K.; Ek, M.; Sheffield, J.; Cosgrove, B.; Wood, E.; Luo, L.; Alonge, C.; Wei, H.; Meng, J. Continental-scale water and energy flux analysis and validation for the north American land data assimilation system project phase 2 (NLDAS-2): 1. Intercomparison and application of model products. *J. Geophys. Res. Atmos.* **2012**, *117*, D03109. [CrossRef]
80. Ek, M.B.; Mitchell, K.E.; Lin, Y.; Rogers, E.; Grunmann, P.; Koren, V.; Gayno, G.; Tarpley, J.D. Implementation of Noah land surface model advances in the National Centers for Environmental Prediction operational mesoscale Eta model. *J. Geophys. Res. Earth Surf.* **2003**, *108*. [CrossRef]
81. Koster, R.D.; Suarez, M.J. *Energy and Water Balance Calculations in the Mosaic LSM*; National Aeronautics and Space Administration, Goddard Space Flight Center, Laboratory for Atmospheres, Data Assimilation Office: Laboratory for Hydrospheric Processes, 1996. Available online: https://permanent.fdlp.gov/gpo60361/19960017819.pdf (accessed on 24 January 2022).
82. Liang, X.; Lettenmaier, D.P.; Wood, E.F.; Burges, S.J. A simple hydrologically based model of land surface water and energy fluxes for general circulation models. *J. Geophys. Res. Earth Surf.* **1994**, *99*, 14415–14428. [CrossRef]
83. Long, D.; Scanlon, B.R.; Longuevergne, L.; Sun, A.Y.; Fernando, D.N.; Save, H. GRACE satellite monitoring of large depletion in water storage in response to the 2011 drought in Texas. *Geophys. Res. Lett.* **2013**, *40*, 3395–3401. [CrossRef]
84. Chen, J.L.; Wilson, C.R.; Tapley, B.; Yang, Z.-L.; Niu, G.-Y. 2005 drought event in the Amazon River basin as measured by GRACE and estimated by climate models. *J. Geophys. Res. Earth Surf.* **2009**, *114*. [CrossRef]
85. Huffman, G.J.; Stocker, E.F.; Bolvin, D.T.; Nelkin, E.J.; Tan, J. *GPM IMERG Final Precipitation l3 1 Month 0.1 Degree × 0.1 Degree V06*; Goddard Earth Sciences Data and Information Services Center: Greenbelt, MD, USA, 2019. Available online: https://disc.gsfc.nasa.gov/datasets/GPM_3IMERGM_06/summary?keywords=%22IMERG%20final%22.V06 (accessed on 1 April 2020).
86. Hennermann, K.; Berrisford, P. *ERA5 Data Documentation*; Copernicus Knowledge Base—ECMWF: Reading, UK, 2020; Available online: https://confluence.ecmwf.int/display/CKB/ERA5%3A+data+documentation (accessed on 24 January 2022).
87. Chen, L.; He, Q.; Liu, K.; Li, J.; Jing, C. Downscaling of GRACE-Derived Groundwater Storage Based on the Random Forest Model. *Remote Sens.* **2019**, *11*, 2979. [CrossRef]
88. Seidou, O.; Asselin, J.J.; Ouarda, T.B.M.J. Bayesian multivariate linear regression with application to change point models in hydrometeorological variables. *Water Resour. Res.* **2007**, *43*. [CrossRef]
89. Kawamoto, A.H.; McClelland, J.L.; Rumelhart, D.E. Explorations in Parallel Distributed Processing: A Handbook of Models, Programs, and Exercises. *Am. J. Psychol.* **1989**, *102*, 435. [CrossRef]
90. Nash, J.E.; Sutcliffe, J.V. River flow forecasting through conceptual models part i—a discussion of principles. *J. Hydrol.* **1970**, *10*, 282–290. [CrossRef]
91. Chowdhury, A.H.; Mace, R.E. *Groundwater Resource Evaluation and Availability Model of the Gulf Coast Aquifer in the Lower Rio Grande Valley of Texas*; Texas Water Development Board: Austin, TX, USA, 2007.
92. Area, H.; Model, G. *Hydrogeology and Simulation of Groundwater Flow and Land-Surface Subsidence in the Northern Part of the Gulf Coast AQ-Uifer System, Texas, 1891–2009*; U.S. Geological Survey: Reston, VI, USA, 2012.
93. Kelley, V.A.; Deeds, N.E.; Fryar, D.G.; Nicot, J.-P. Groundwater Availability Models for the Queen City and Sparta Aquifers. For the Texas Water Development Board: INTERA Incorporated. 2004. Available online: http://www.twdb.texas.gov/groundwater/models/gam/qcsp/QCSP_Model_Report.pdf (accessed on 1 June 2020).
94. Hutchison, W.R.; Hill, M.E.; Anaya, R.; Hassan, M.M.; Oliver, W.; Jigmond, M.; Wade, S.; Aschenbach, E. Groundwater Management Area 16 Groundwater Flow Model. Texas Water Development Board. 2011. Available online: https://www.twdb.texas.gov/groundwater/models/alt/gma16/GMA16_Model_Report_DRAFT.pdf (accessed on 1 June 2020).
95. Ryder, P.D.; Ardis, A.F. *Hydrology of the Texas Gulf Coast Aquifer Systems*; U.S. Geological Survey: Reston, VI, USA, 1991.

96. Sun, A.Y.; Green, R.; Rodell, M.; Swenson, S. Inferring aquifer storage parameters using satellite and in situ measurements: Estimation under uncertainty. *Geophys. Res. Lett.* **2010**, *37*. [CrossRef]
97. Zhong, Y.; Zhong, M.; Feng, W.; Zhang, Z.; Shen, Y.; Wu, D. Groundwater Depletion in the West Liaohe River Basin, China and Its Implications Revealed by GRACE and In Situ Measurements. *Remote Sens.* **2018**, *10*, 493. [CrossRef]
98. Rahaman, M.; Thakur, B.; Kalra, A.; Li, R.; Maheshwari, P. Estimating High-Resolution Groundwater Storage from GRACE: A Random Forest Approach. *Environments* **2019**, *6*, 63. [CrossRef]
99. Zeileis, A.; Kleiber, C.; Krämer, W.; Hornik, K. Testing and dating of structural changes in practice. *Comput. Stat. Data Anal.* **2003**, *44*, 109–123. [CrossRef]
100. Bai, J.; Perron, P. Computation and analysis of multiple structural change models. *J. Appl. Econ.* **2002**, *18*, 1–22. [CrossRef]
101. Forkel, M.; Carvalhais, N.; Verbesselt, J.; Mahecha, M.D.; Neigh, C.S.R.; Reichstein, M. Trend Change Detection in NDVI Time Series: Effects of Inter-Annual Variability and Methodology. *Remote Sens.* **2013**, *5*, 2113–2144. [CrossRef]
102. Hastings, W.K. Monte Carlo sampling methods using Markov chains and their applications. *Biometrika* **1970**, *57*, 97–109. [CrossRef]
103. Vrugt, J.A.; ter Braak, C.; Diks, C.; Robinson, B.A.; Hyman, J.M.; Higdon, D. Accelerating Markov Chain Monte Carlo Simulation by Differential Evolution with Self-Adaptive Randomized Subspace Sampling. *Int. J. Nonlinear Sci. Numer. Simul.* **2009**, *10*, 273–290. [CrossRef]
104. Cleaveland, M.K.; Votteler, T.H.; Stahle, D.K.; Casteel, R.C.; Banner, J.L. Extended chronology of drought in south central, southeastern and west Texas. *Tex. Water J.* **2011**, *2*, 54–96.
105. United States. National Weather Service. Major South Texas Storm Events. Available online: https://www.weather.gov/crp/stormhistory (accessed on 1 January 2022).
106. Houborg, R.; Rodell, M.; Li, B.; Reichle, R.; Zaitchik, B. Drought indicators based on model-assimilated Gravity Recovery and Climate Experiment (GRACE) terrestrial water storage observations. *Water Resour. Res.* **2012**, *48*. [CrossRef]
107. Xiao, R.; He, X.; Zhang, Y.; Ferreira, V.; Chang, L. Monitoring Groundwater Variations from Satellite Gravimetry and Hydrological Models: A Comparison with in-situ Measurements in the Mid-Atlantic Region of the United States. *Remote Sens.* **2015**, *7*, 686–703. [CrossRef]
108. Syed, T.H.; Famiglietti, J.S.; Rodell, M.; Chen, J.; Wilson, C.R. Analysis of terrestrial water storage changes from GRACE and GLDAS. *Water Resour. Res.* **2008**, *44*, W02433. [CrossRef]
109. Meng, F.; Su, F.; Li, Y.; Tong, K. Changes in Terrestrial Water Storage During 2003–2014 and Possible Causes in Tibetan Plateau. *J. Geophys. Res. Atmos.* **2019**, *124*, 2909–2931. [CrossRef]
110. Thomas, B.F.; Famiglietti, J.S. Identifying Climate-Induced Groundwater Depletion in GRACE Observations. *Sci. Rep.* **2019**, *9*, 4124. [CrossRef]
111. Lohman, S.W. *Definitions of Selected Ground-Water Terms, Revisions and Conceptual Refinements*; U.S. Government Printing Office: Washington, DC, USA, 1972; pp. 1–21. [CrossRef]
112. Roy, D.K.; Bithin, D. Comparative efficiency of different artificial intelligence-based models for predicting density dependent saltwater intrusion processes in coastal aquifers and saltwater intrusion management utilizing the best performing model. *Desalination Water Treat.* **2018**, *105*, 160–180. [CrossRef]
113. Falkenmark, M. Freshwater as shared between society and ecosystems: From divided approaches to integrated challenges. *Philos. Trans. R. Soc. B Biol. Sci.* **2003**, *358*, 2037–2049. [CrossRef]